



Article

A New Pabs Model for Quantitatively Diagnosing Phosphorus Nutritional Status in Corn Plants

Xinwei Zhao , Shengbo Chen *, Yucheng Xu  and Zibo Wang

College of Geo-Exploration Science and Technology, Jilin University, Changchun 130026, China; xinwei22@mails.jlu.edu.cn (X.Z.); ycxu21@mails.jlu.edu.cn (Y.X.); zbwang22@mails.jlu.edu.cn (Z.W.)

* Correspondence: chensb@jlu.edu.cn

Abstract: Accurate diagnosis of plant phosphorus nutritional status is critical for optimizing agricultural practices and enhancing resource efficiency. Existing methods are limited to qualitatively assessing plant phosphorus nutritional status and cannot quantitatively estimate the plant's phosphorus requirements. Moreover, these methods are time-consuming, making them impractical for large-scale application. In this study, we developed an advanced phosphorus absorption model (Pabs) that integrates the phosphorus nutrition index (PNI) and phosphorus use efficiency (PUE). The PUE, a critical metric for assessing phosphate fertilizer use efficiency, was quantified by comparing yields under fertilized and unfertilized conditions. Utilizing the Agricultural Production Systems Simulator (APSIM) model, we simulated maize (*Zea mays* L.) phosphorus concentration (P) and aboveground biomass (Bio) under varying phosphorus application rates. The model exhibited robust performance, achieving an R^2 above 0.95 and an RMSE below 0.22. Based on the APSIM model simulations, a phosphorus dilution curve ($P_c = 3.17 \text{ Bio}^{-0.29}$, $R^2 = 0.98$) was established, reflecting the dilution trends of phosphorus across growth stages. Furthermore, the use of vegetation indices (VIS) to evaluate phosphorus nutritional status also showed promising results, with inversion accuracies exceeding 0.70. To validate the model, field sampling was conducted in maize-growing regions of Changchun. Results demonstrated a correct diagnosis rate of 75%, underscoring the model's capacity to accurately estimate phosphorus requirements on a regional scale. These findings highlight the Pabs model as a reliable tool for precision phosphorus management, offering significant potential to optimize fertilization strategies and support sustainable agricultural systems.

Keywords: phosphorus status diagnosis; precision phosphorus management; phosphorus absorption model; phosphorus nutrition index; agricultural production systems simulator



Academic Editors: Rui Sun, Jiang Chen and Wen Zhuo

Received: 28 November 2024

Revised: 12 January 2025

Accepted: 13 January 2025

Published: 14 January 2025

Citation: Zhao, X.; Chen, S.; Xu, Y.; Wang, Z. A New Pabs Model for Quantitatively Diagnosing Phosphorus Nutritional Status in Corn Plants. *Appl. Sci.* **2025**, *15*, 764. <https://doi.org/10.3390/app15020764>

Copyright: © 2025 by the authors. Licensee MDPI, Basel, Switzerland. This article is an open access article distributed under the terms and conditions of the Creative Commons Attribution (CC BY) license (<https://creativecommons.org/licenses/by/4.0/>).

1. Introduction

Phosphorus is essential for regulating plant physiological processes and enhancing tolerance to abiotic stresses, such as heat, salinity, drought, waterlogging, elevated CO₂, and heavy metal toxicity [1,2]. Plants are capable of sensing changes in phosphorus availability and responding through specific signaling pathways, adjustments in root architecture, and modifications in stomatal morphology [3,4]. A deeper understanding of how plants perceive and respond to phosphorus availability is vital for developing strategies to improve crop yield and stress resilience. Phosphorus also plays a critical role in key metabolic and physiological processes, such as energy metabolism, ATP, DNA synthesis, cell division, and phospholipid biosynthesis, primarily in the form of phosphate (Pi) or Pi esters [5]. A deficiency in Pi severely impacts root development, vegetative growth, fruit production,

and quality, ultimately leading to a decrease in crop yields [6–8]. Therefore, precision in phosphorus fertilizer application and effective management strategies are paramount for optimizing production.

Plant phosphorus concentration (P) is a widely recognized indicator of crop phosphorus nutritional status. To enhance the precision of phosphorus diagnostics, the critical phosphorus concentration (P_c) concept was introduced, representing the minimum phosphorus level required to achieve maximum aboveground biomass (Bio). P_c decreases as biomass increases, and their relationship is described by a negative power function, forming the critical P dilution curve [9,10]. This curve allows for the determination of P_c at any given biomass. Researchers worldwide have developed critical phosphorus concentration dilution curve models for various crops in different regions, climate conditions, and environments. For example, critical phosphorus dilution models have been established for potato (*Solanum tuberosum* L.) [9,11], cotton (*Gossypium hirsutum* L.) [12], and Timothy grass (*Phleum pratense* L.) [13], with corresponding models as follows: $P_c = 3.92 \text{ Bio}^{-0.30}$ and $P_c = 5.23 \text{ Bio}^{-0.19}$, $P_c = 7.84 \text{ Bio}^{-0.22}$ and $P_c = 7.74 \text{ Bio}^{-0.20}$, and $P_c = 5.23 \text{ Bio}^{-0.40}$ and $P_c = 3.27 \text{ Bio}^{-0.20}$, respectively. The comparison of P to P_c , expressed as the phosphorus nutritional index (PNI), provides a robust assessment of phosphorus supply status. However, PNI calculations traditionally involve destructive sampling and chemical analysis, which are time-intensive, costly, and impractical for large-scale applications, akin to the nitrogen nutrition index (NNI) [14].

In nitrogen nutrition research, combining vegetation indices (VIs) with NNI has emerged as an efficient, non-destructive diagnostic approach. This method leverages remote sensing technologies to assess nitrogen content rapidly and accurately, facilitating effective management in large-scale agricultural systems, such as rice (*Oryza sativa* L.), wheat (*Triticum aestivum* L.), and maize (*Zea mays* L.). For example, GreenSeeker NDVI and RVI explained 47% and 44% of the variability in winter wheat NNI across different sites and growth stages, respectively, demonstrating their effectiveness in nitrogen monitoring [15]. Additionally, using two vegetation indices—Green Re-normalized Difference Vegetation Index (GRDVI) and Modified Green Soil Adjusted Vegetation Index (MGSAVI)—was effective in estimating winter wheat NNI across various site years and growth stages, achieving an R^2 value between 0.77 and 0.78 [16]. For rice, the GreenSeeker system explained 25–34% of NNI variability at the stem elongation stage and 30–31% at the heading stage, indicating the relevance of growth-stage-specific nitrogen assessments [16]. Furthermore, four red-edge based indices—Red Edge Soil Adjusted Vegetation Index (RESAVI), Modified RESAVI (MRESAVI), Red Edge Difference Vegetation Index (REDVI), and Red Edge Re-normalized Difference Vegetation Index (RERDVI)—showed similar effectiveness in estimating rice NNI across growth stages, with an R^2 of 0.76 [17]. These results highlight the importance of VIs in optimizing nitrogen management, reducing excessive nitrogen applications, and improving fertilizer efficiency.

Phosphorus nutrition diagnostics remain less explored compared to nitrogen monitoring, with existing methods such as soil testing and tissue analysis presenting notable limitations. Soil testing, which offers insights into available phosphorus in the soil, is typically used for proactive fertility management before planting and is based on correlations between nutrient levels and crop yield responses [18]. However, it has significant drawbacks, primarily due to its reliance on a single snapshot of soil phosphorus status, which fails to capture the temporal variations in phosphorus availability throughout the growing season. Additionally, the accuracy of soil tests is influenced by the testing method and variability in soil sampling across large areas, resulting in inconsistencies. Similarly, while tissue analysis is crucial for evaluating phosphorus status during the growing season, it too has limitations. It can only be conducted when the crop is actively growing, and

even if phosphorus deficiencies are detected, the effectiveness of in-season amendments remains uncertain because phosphorus is immobile in the soil, limiting plant access to added nutrients [19]. Moreover, interpreting phosphorus tissue concentrations is challenging as the critical and sufficiency ranges—representing nutrient concentrations below which yield responses occur and where added nutrients no longer increase yield but can still influence nutrient levels—vary by growth stage and plant part [20]. These complexities make it difficult to apply tissue analysis consistently across different growth stages and plant parts, limiting its practical use in large-scale phosphorus management for crops such as corn. Together, these challenges highlight the need for alternative, dynamic, and real-time phosphorus-monitoring systems. The combination of VIs and PNI offers a promising solution, enabling continuous, non-destructive monitoring of phosphorus status throughout the growing season. By integrating these indices, it becomes possible to capture the temporal fluctuations in phosphorus availability and better align fertilization practices with the crop's actual nutrient requirements, thus improving phosphorus use efficiency and minimizing environmental impact.

This study investigates the potential of vegetation indices for estimating phosphorus nutritional status under varying phosphorus fertilizer levels. The objectives of the research are as follows: (i) to assess the relationship between vegetation indices and phosphorus nutritional status in maize under different fertilizer treatments and (ii) to construct a phosphorus absorption (Pabs) model for regional-scale phosphorus optimization and quantitative phosphorus nutrition diagnostics. The findings provide a theoretical framework for improving phosphorus management in maize, with practical implications for reducing fertilizer inputs and promoting sustainable agricultural practices.

2. Materials and Methods

2.1. Experimental Design

This study was conducted at the Agricultural Experimental Base of Jilin University in Changchun City, Jilin Province, China, situated within the coordinates 43°05′–45°15′ N and 124°18′–127°02′ E (Figure 1). This region, characterized by flat terrain and fertile black soil, is highly conducive to crop cultivation. During the 2023 corn-growing season, the research integrated remote sensing observations and ground-based biochemical measurements to assess phosphorus fertilization in maize (Xianyu 335). Four phosphorus application levels—0, 50, 100, and 150 kg/ha—were applied based on local soil phosphorus conditions and prior experimental data, with additional nutrient supply of 220 kg/ha nitrogen and 100 kg/ha potassium incorporated before sowing. Each phosphorus treatment was repeated in four groups, resulting in a total of 16 experimental units, from which 96 samples were collected. Data collection was conducted across key growth stages of maize, including jointing, large trumpet, tasseling, silking, grain formation, and milk maturity, with a focus on critical indicators, such as canopy spectral data, plant phosphorus concentration, and aboveground biomass. Canopy spectral data were obtained using a FieldSpec 3 Hi-Res Pro portable spectrometer, manufactured by Analytical Spectral Devices, Inc. (ASD) in Longmont, CO, USA, with measurements taken between 10:00 and 14:00 under clear weather conditions and minimal wind (≤ 2 m/s). The spectrometer sensor was positioned 1 m above the canopy, at a 25° field of view angle, covering a ground area with a diameter of 0.22 m. Spectral readings, which were averaged from ten measurements per sampling point, were repeated three times per treatment to ensure accuracy in calculating the mean canopy reflectance. Calibration with a standard whiteboard was performed before and after each measurement set to minimize measurement errors. For biomass estimation, three representative maize plants from each plot were selected, and their plant organs were separated and dried at 105 °C for 30 min to kill green tissue, followed by drying at

75 °C until a constant weight was achieved. The resulting dry weight was recorded to calculate biomass per unit area. Phosphorus concentration in plant tissues was determined by grinding the samples through a 0.425 mm sieve, followed by digestion using an H₂SO₄-H₂O₂ method and subsequent vanadate–molybdate colorimetric analysis.

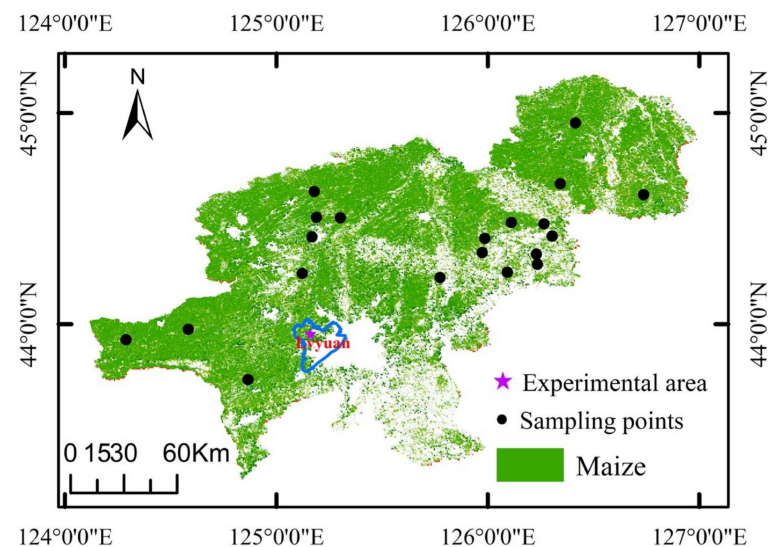


Figure 1. The geographical location of the experimental area.

2.2. Data

In this study, multispectral data for calculating vegetation indices were sourced from Google Earth Engine (<https://earthengine.google.com> (accessed on 1 July 2024)). Sentinel-2, offering high-spatial-resolution optical imagery at 10 m resolution in both visible and near-infrared bands, is well-suited for large-scale environmental monitoring, agricultural assessments, and vegetation analysis [21].

For maize classification in Changchun, a 10 m resolution crop type map was utilized, derived from Sentinel-2 imagery and processed using a random forest algorithm on the Google Earth Engine platform [22].

Climate data, including daily maximum (T_{max}) and minimum (T_{min}) temperatures, precipitation (Rain), solar radiation (SRAD), relative humidity (RH), wind speed (WS), and potential evaporation (PET), were retrieved from the China Meteorological Administration platform (<http://data.cma.cn/> (accessed on 1 May 2024)). These parameters were integral to APSIM model simulations, facilitating an in-depth analysis of crop responses to climate variability [23].

3. Methodology

The workflow of this study, as illustrated in Figure 2, outlines the steps involved in simulating key agronomic indicators and developing models for phosphorus nutrition and biomass in maize. Measurements were taken at six critical growth stages—jointing, large trumpet, tasseling, silking, grain formation, and milk maturity—across four phosphorus application levels (0, 50, 100, and 150 kg/ha), with each treatment replicated four times. To ensure the accuracy and reliability of the data, special attention was given to the timing of data collection, the phenological phase of maize, and the number of replications. Instruments were calibrated before and after each session, and standard procedures were followed to minimize environmental and procedural errors, ensuring consistency across all measurements. This rigorous approach allowed for the accurate reflection of phosphorus dynamics and maize's response to varying phosphorus application levels throughout the growing season. The data collected, including canopy spectral data, plant phosphorus

concentration, and aboveground biomass, were integrated with Sobol sensitivity analysis to identify the vegetation index most strongly correlated with these indicators. These results formed the basis for developing inversion models for both maize's aboveground biomass and phosphorus concentration, contributing to the construction of a phosphorus nutritional index (PNI) model. Additionally, the agricultural production systems simulator (APSIM) model was employed to simulate phosphorus concentration and biomass, with the simulation results forming the foundation for developing the critical phosphorus concentration (Pc) model. To enhance the model's accuracy, phosphorus use efficiency (PUE) was incorporated, leading to the development of the phosphorus absorption (Pabs) model, which facilitated the quantitative monitoring of phosphorus concentration in maize throughout the growing season in Changchun.

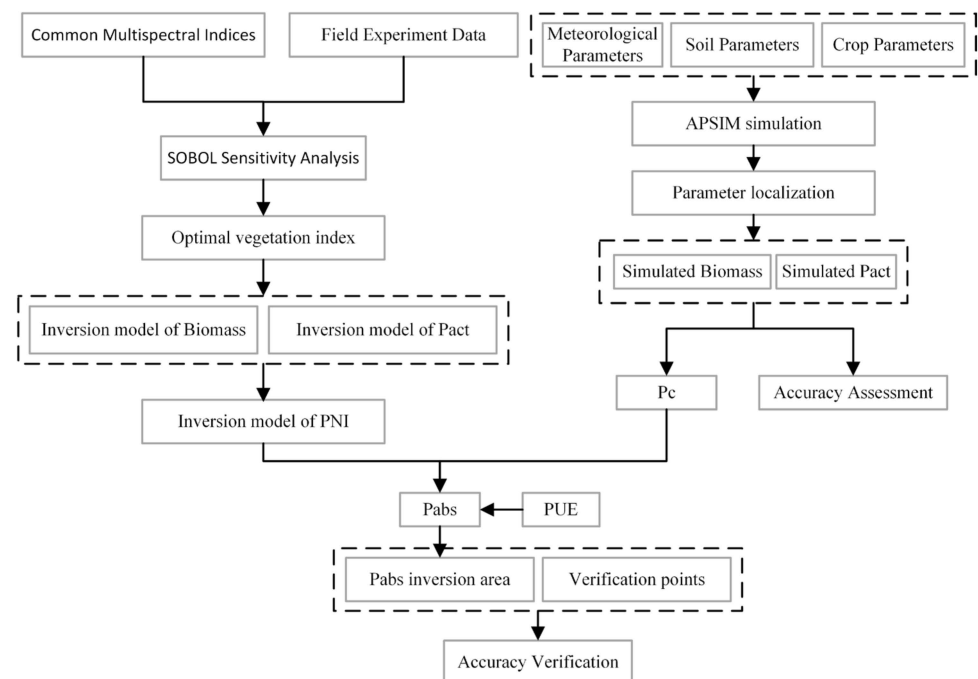


Figure 2. Flowchart of this study.

3.1. Sobol Sensitivity Analysis

Numerous spectral indices have been developed to estimate key plant biophysical variables, including chlorophyll concentration, leaf area index, and biomass. This study employed Sentinel-2 satellite imagery to explore the potential of vegetation indices in assessing maize phosphorus status. A comprehensive analysis was conducted on 50 vegetation indices (Table 1; [24–45]).

Table 1. Multispectral vegetation index.

Vegetation Index	Formula	Ref.
Two-band vegetation indices		
Ratio Vegetation Index 1 (RVI1)	NIR/B	[24]
Ratio Vegetation Index 2 (RVI2)	NIR/G	[25]
Ratio Vegetation Index 3 (RVI3)	NIR/R	[24]
Difference Index1 (DVI1)	$\text{NIR} - \text{B}$	[24]
Difference Index2 (DVI2)	$\text{NIR} - \text{G}$	[24]
Difference Index3 (DVI3)	$\text{NIR} - \text{R}$	[24]

Table 1. Cont.

Vegetation Index	Formula	Ref.
Normalized Difference Vegetation Index 1 (NDVI1)	$(\text{NIR} - \text{R})/(\text{NIR} + \text{R})$	[25]
Normalized Difference Vegetation Index 2 (NDVI2)	$(\text{NIR} - \text{G})/(\text{NIR} + \text{G})$	[26]
Normalized Difference Vegetation Index 3 (NDVI3)	$(\text{NIR} - \text{B})/(\text{NIR} + \text{B})$	[25]
Renormalized Difference Vegetation Index 1 (RDVI1)	$(\text{NIR} - \text{B})/\text{SQRT}(\text{NIR} + \text{B})$	[27]
Renormalized Difference Vegetation Index 2 (RDVI2)	$(\text{NIR} - \text{G})/\text{SQRT}(\text{NIR} + \text{G})$	[27]
Renormalized Difference Vegetation Index 3 (RDVI3)	$(\text{NIR} - \text{R})/\text{SQRT}(\text{NIR} + \text{R})$	[27]
Wide Dynamic Range Vegetation Index 1 (WDRVI1)	$(0.12 \text{ NIR} - \text{R})/(0.12 \cdot \text{NIR} + \text{R})$	[28]
Wide Dynamic Range Vegetation Index 2 (WDRVI2)	$(0.12 \text{ NIR} - \text{G})/(0.12 \cdot \text{NIR} + \text{G})$	[28]
Wide Dynamic Range Vegetation Index 3 (WDRVI3)	$(0.12 \text{ NIR} - \text{B})/(0.12 \cdot \text{NIR} + \text{B})$	[28]
Soil Adjusted Vegetation Index (SAVI)	$1.5(\text{NIR} - \text{R})/(\text{NIR} + \text{R} + 0.5)$	[29]
Optimization of soil-adjusted VI (OSAVI)	$(1 + 0.16)(\text{NIR} - \text{R})/(\text{NIR} + \text{R} + 0.16)$	[30]
Green Soil Adjusted Vegetation Index (GSAVI)	$1.5(\text{NIR} - \text{G})/(\text{NIR} + \text{G} + 0.5)$	[29]
Blue Soil Adjusted Vegetation Index (BSAVI)	$1.5(\text{NIR} - \text{B})/(\text{NIR} + \text{B} + 0.5)$	[29]
Modified Simple Ratio (MSR)	$(\text{NIR}/\text{R} - 1)/\text{SQRT}(\text{NIR}/\text{R} + 1)$	[31]
Green Optimal Soil Adjusted Vegetation Index (G0SAVI)	$(1 + 0.16)(\text{NIR} - \text{G})/(\text{NIR} + \text{G} + 0.16)$	[30]
Blue Optimal Soil Adjusted Vegetation Index (BOSAVI)	$(1 + 0.16)(\text{NIR} - \text{B})/(\text{NIR} + \text{B} + 0.16)$	[30]
Modified Soil Adjusted Vegetation Index (MSAVI)	$0.5[2 \cdot \text{NIR} + 1 - \text{SQRT}[(2 \cdot \text{NIR} + 1)^2 - 8(\text{NIR} - \text{R})]]$	[32]
Modified Green Soil Adjusted Vegetation Index (MGSAVI1)	$0.5[2 \cdot \text{NIR} + 1 - \text{SQRT}[(2 \cdot \text{NIR} + 1)^2 - 8(\text{NIR} - \text{G})]]$	[32]
Modified Blue Soil Adjusted Vegetation Index (MBSAVI)	$0.5[2 \cdot \text{NIR} + 1 - \text{SQRT}[(2 \cdot \text{NIR} + 1)^2 - 8(\text{NIR} - \text{B})]]$	[32]
Three-band vegetation indices		
Simple Ratio Vegetation Index (SR)	$\text{R}/\text{G} \times \text{NIR}$	[33]
Modified Normalized Difference Vegetation Index 1 (mNDVI1)	$(\text{NIR} - \text{R} + 2 \cdot \text{G})/(\text{NIR} + \text{R} - 2 \cdot \text{G})$	[34]
Modified Normalized Difference Vegetation Index 2 (mNDVI2)	$(\text{NIR} - \text{R} + 2 \cdot \text{B})/(\text{NIR} + \text{R} - 2 \cdot \text{B})$	[34]
New Modified Simple Ratio (mSR)	$(\text{NIR} - \text{B})/(\text{R} - \text{B})$	[35]
Visible Atmospherically Resistant Index (VARI)	$(\text{G} - \text{R})/(\text{G} + \text{R} - \text{B})$	[36]
Structure Insensitive Pigment Index (SIPI)	$(\text{NIR} - \text{B})/(\text{NIR} - \text{R})$	[37]
Structure Insensitive Pigment Index 1 (SIPI1)	$(\text{NIR} - \text{B})/(\text{NIR} - \text{G})$	[37]
Normalized Different Index (NDI)	$(\text{NIR} - \text{R})/(\text{NIR} - \text{G})$	[33]
Plant Senescence Reflectance Index (PSRI)	$(\text{R} - \text{B})/\text{NIR}$	[35]
Modified nonlinear VI (MNVI)	$1.5(\text{NIR}^2 - \text{G})/(\text{NIR}^2 + \text{R} + 0.5)$	[38]
Plant Senescence Reflectance Index 1 (PSRI1)	$(\text{R} - \text{G})/\text{NIR}$	[35]
Triangular Vegetation Index (TVI)	$0.5 [120 (\text{NIR} - \text{G}) - 200 (\text{R} - \text{G})]$	[39]
Modified Triangular Vegetation Index 1 (MTVI1)	$1.2 [1.2 (\text{NIR} - \text{G}) - 2.5 (\text{R} - \text{G})]$	[40]
Modified Triangular Vegetation Index 2 (MTVI2)	$1.5 [1.2 (\text{NIR} - \text{G}) - 2.5 (\text{R} - \text{G})]/\text{SQRT} [(2 \cdot \text{NIR} + 1)^2 - (6 \cdot \text{NIR} - 5 \cdot \text{SQRT}(\text{R}) - 0.5)]$	[40]
Modified Triangular Vegetation Index 3 (MTVI3)	$1.5 [1.2 (\text{NIR} - \text{B}) - 2.5 (\text{R} - \text{B})]/\text{SQRT} [(2 \cdot \text{NIR} + 1)^2 - (6 \cdot \text{NIR} - 5 \cdot \text{SQRT}(\text{R}) - 0.5)]$	[40]
Enhanced Vegetation Index (EVI)	$2.5(\text{NIR} - \text{R})/(1 + \text{NIR} + 6\text{R} - 7.5\text{B})$	[41]
Triangular Chlorophyll Index (TCI)	$1.2(\text{NIR} - \text{G}) - 5(\text{R} - \text{G})(\text{NIR}/\text{R})^{0.5}$	[42]
Modified Chlorophyll Absorption in Reflectance Index (MCARI)	$[(\text{NIR} - \text{R}) - 0.2(\text{R} - \text{G})] \times (\text{NIR}/\text{R})$	[43]
Modified Chlorophyll Absorption in Reflectance Index 1 (MCARI1)	$1.2 [2.5 (\text{NIR} - \text{R}) - 1.3 (\text{NIR} - \text{G})]$	[40]
Modified Chlorophyll Absorption in Reflectance Index 2 (MCARI2)	$1.2 [2.5 (\text{NIR} - \text{R}) - 1.3 (\text{R} - \text{G})]/\text{SQRT} [(2 \cdot \text{NIR} + 1)^2 - (6 \cdot \text{NIR} - 5 \cdot \text{SQRT}(\text{R}) - 0.5)]$	[40]
Transformed Chlorophyll Absorption in Reflectance Index (TCARI)	$3 [(\text{NIR} - \text{R}) - 0.2 (\text{NIR} - \text{G})(\text{NIR}/\text{R})]$	[44]
TCARI/OSAVI	TCARI/OSAVI	[44]
MCARI/MTVI2	MCARI/MTVI2	[45]
TCARI/MSAVI	TCARI/MSAVI	[44]
TCI/OSAVI	TCI/OSAVI	[42]

In this study, the Sobol sensitivity analysis was employed to assess the influence of input variables on the performance of the LIBSVM surrogate model. The Sobol method decomposes the variance of the output to calculate the first-order sensitivity index (S) and total effect index (ST) for each input parameter.

3.2. APSIM Model

Model simulations allow for the quantitative assessment of how different environmental conditions and management practices influence corn phosphorus concentration and aboveground biomass. The agricultural production systems simulation (APSIM) model is widely recognized for its flexibility and accuracy in simulating crop growth and nutrient cycling. Over the years, APSIM has been used to evaluate corn growth under various fertilization and irrigation strategies, with a particular focus on phosphorus uptake efficiency and its contribution to biomass accumulation [46]. In this study, APSIM was utilized to simulate two key agronomic indicators—plant phosphorus concentration and aboveground biomass—across critical growth stages: jointing, trumpet, tasseling, silking, grain formation, and milk ripening. The model incorporated variety-specific genetic parameters, with scenario and field trial settings remaining consistent throughout the experiment. Calibration and validation were conducted using experimental data, with parameter adjustments made through a “trial-and-error” approach.

3.3. Model Construction

3.3.1. Phosphorus Dilution Curve

The phosphorus dilution curve (Pc) model was defined according to the method outlined in [11], and the model construction approach proposed by Belanger et al. [10] was applied to develop the critical dilution curve model, as expressed in Equation (1):

$$P_c = a * Bio^{-b}, \quad (1)$$

where a represents the phosphorus concentration of the plant when the aboveground biomass is 1 t/ha; Bio is the aboveground biomass of the plant, measured in t/ha; and b is the statistical parameter controlling the slope of the curve.

3.3.2. Phosphorus Nutrition Index

The phosphorus nutrition index (PNI) [11] is calculated as shown in Equation (2):

$$PNI = P/P_c, \quad (2)$$

where P_c is the percentage of the critical phosphorus concentration of the plant in dry matter, and P is the percentage of the actual measured phosphorus concentration of the plant in dry matter.

3.3.3. The Pabs Model

To enhance the timeliness of crop phosphorus nutrition diagnosis and support large-scale phosphorus management, we developed a corn phosphorus absorption (Pabs) model. The phosphorus standard accumulation (P_{sa}) and phosphorus actual accumulation (P_{aa}) in corn plants were calculated by multiplying the critical phosphorus concentration (P_c) and the plant's phosphorus concentration (P) by its aboveground biomass (Bio), as shown in Equations (3) and (4):

$$P_{sa} = a * Bio^{1-b}, \quad (3)$$

$$P_{aa} = P * Bio, \quad (4)$$

The Pabs model was derived by subtracting the standard phosphorus accumulation from the actual phosphorus accumulation, as indicated in Equation (5):

$$Pabs = (1 - PNI) \left(a * Bio^{1-b} \right), \quad (5)$$

where 1 represents the value of PNI under the optimal phosphorus nutrition state of the plant [11], recorded as PNI_{target} .

To further optimize the model's accuracy, we incorporated the phosphorus use efficiency (PUE) [47], as given by Equation (6):

$$PUE = \frac{(AP - PB)}{PF} \times 100\% \quad (6)$$

where AP represents the treatment of corn with phosphorus fertilizer, PB represents the treatment of corn without phosphorus fertilizer, PF is the amount of phosphorus fertilizer used for corn, and the value of PAE in this study is 37%.

The final optimized phosphorus absorption model is represented in Equation (7):

$$P_{abs} = \frac{a * Bio^{1-b} (PNI_{target} - PNI)}{PUE} \quad (7)$$

4. Results

4.1. Establishment of P_c

The APSIM model demonstrated strong performance in simulating two key agronomic indicators: plant phosphorus concentration (Figure 3a) and aboveground biomass (Figure 3b). For plant phosphorus concentration, the model achieved a high coefficient of determination ($R^2 = 0.967$) and a low root mean square error (RMSE = 0.027), indicating a strong agreement between observed and simulated values, with minimal deviations. Similarly, for aboveground biomass, the model exhibited robust predictive accuracy, with an R^2 of 0.956 and an RMSE of 0.219. These results highlight the model's ability to accurately reflect the dynamics of phosphorus uptake and biomass accumulation in maize. Figure 3a illustrates the linear relationship between observed and simulated plant phosphorus concentrations, where the regression Equation $y = 0.986x + 0.039$ closely aligns the two datasets. In Figure 3b, the relationship between observed and simulated aboveground biomass is represented by this Equation: $y = 0.905x + 1.091$, further demonstrating the model's strong predictive capability. Both diagrams show data points closely distributed along the 1:1 line, emphasizing the consistency of the model's simulations across a wide range of values. These findings suggest that, with localized parameter adjustments, the APSIM model effectively simulates both plant phosphorus concentration and aboveground biomass within acceptable ranges.

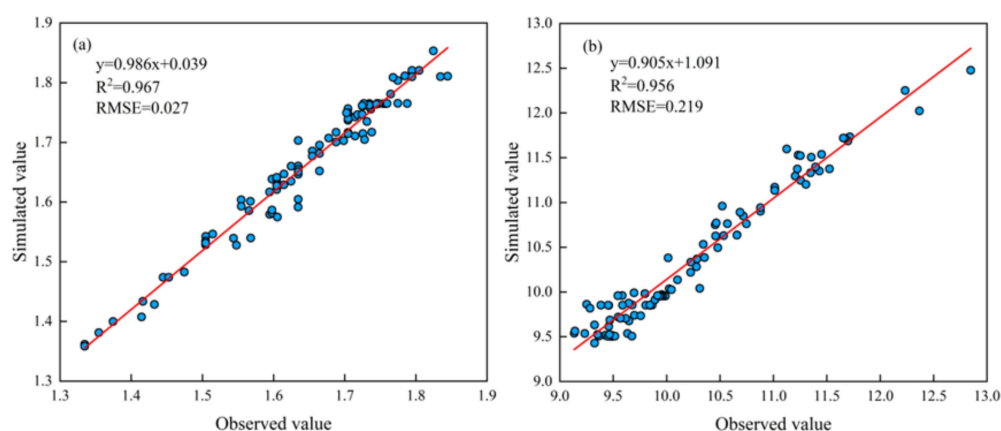


Figure 3. Comparison between measured and simulated values: (a) phosphorus concentration and (b) aboveground biomass.

Variance analysis was conducted on simulated data for plant aboveground biomass and phosphorus concentration across six growth stages: jointing, trumpet, tasseling, silking, grain formation, and milk maturity. This analysis identified phosphorus-sufficient and phosphorus-deficient points, with phosphorus-deficient points defined as those where biomass significantly increased with phosphorus application, and phosphorus-sufficient points showing no such increase. For phosphorus-deficient points, biomass within the same growth stage was plotted as the x -axis and the corresponding phosphorus concentration as the y -axis. Linear fitting was applied to derive a regression line. The average biomass of phosphorus-sufficient points was considered the maximum biomass, and a vertical line was drawn from this value on the regression line. The intersection of the vertical line with the regression line determined the minimum phosphorus concentration required for maximum growth, defined as the critical phosphorus concentration. The P_c values for the jointing, trumpet, tasseling, silking, grain formation, and milk maturity stages were calculated as 2.44, 2.05, 1.82, 1.66, 1.45, and 1.27 g/kg, respectively, with corresponding biomass values of 2.14, 4.52, 6.75, 9.32, 13.58, and 18.24 t/ha. These P_c values were then fitted against the maximum aboveground biomass to establish the P_c model (Figure 4). The coefficient of determination (R^2) for the model was 0.98, indicating an extremely high level of significance ($p < 0.001$).

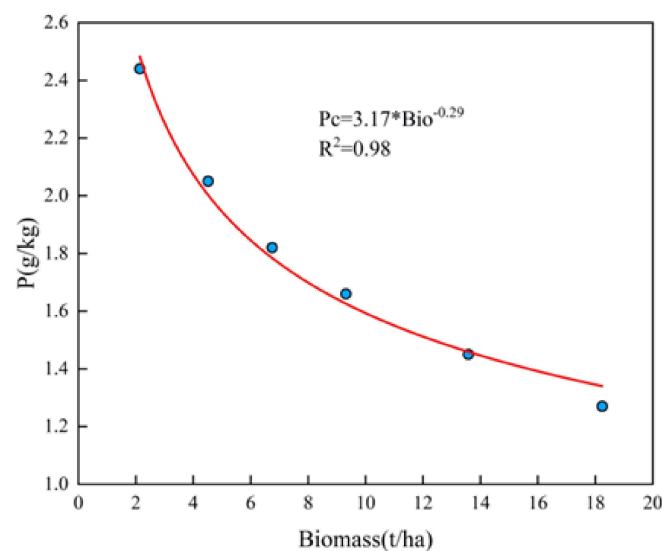


Figure 4. P dilution curves model.

4.2. Sobol Sensitivity Analysis

Figures 5 and 6 illustrate the predictive accuracy of the LIBSVM model in identifying optimal vegetation indices related to maize phosphorus concentration and aboveground biomass. For phosphorus concentration, the model performed well in the training set (Figure 5a), achieving an R^2 of 0.834 and an RMSE of 0.048, indicating high fitting accuracy. However, in the test set (Figure 5b), the R^2 decreased to 0.615, explaining 61.5% of the variance, while a higher RMSE of 0.073 suggested greater prediction errors and lower accuracy and reliability during testing. For aboveground biomass prediction, the model exhibited superior performance in the training set (Figure 6a), with an R^2 of 0.838 and an RMSE of 0.322, explaining 83.8% of the variance. In the test set (Figure 6b), the R^2 remained relatively high at 0.770, explaining 77.0% of the variance, but the RMSE increased to 0.368, indicating larger prediction errors and reduced accuracy during testing. While the predictive performance for both variables was moderate during the testing phase, the model's strong performance in the training phase and overall robustness highlight its reliability and potential for sensitivity analysis and vegetation index selection.

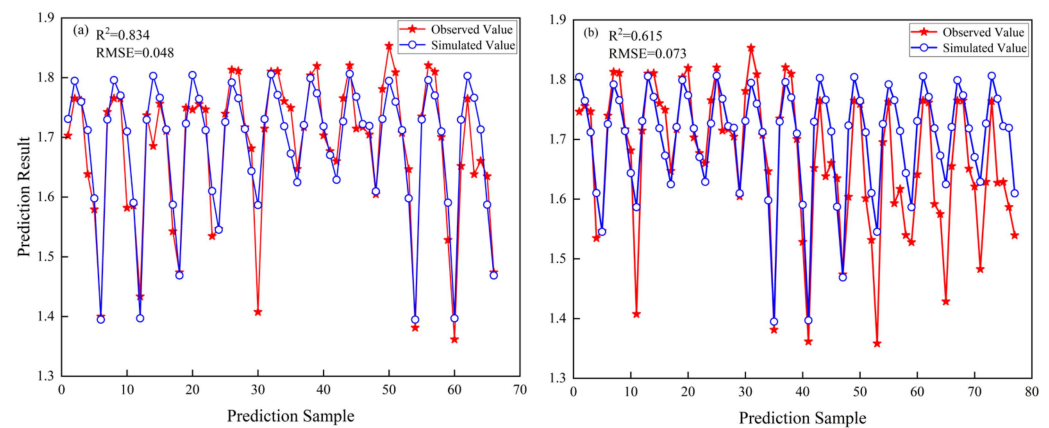


Figure 5. Comparison of predicted plant phosphorus concentration: (a) LIBSVM proxy model training set; (b) testing set.

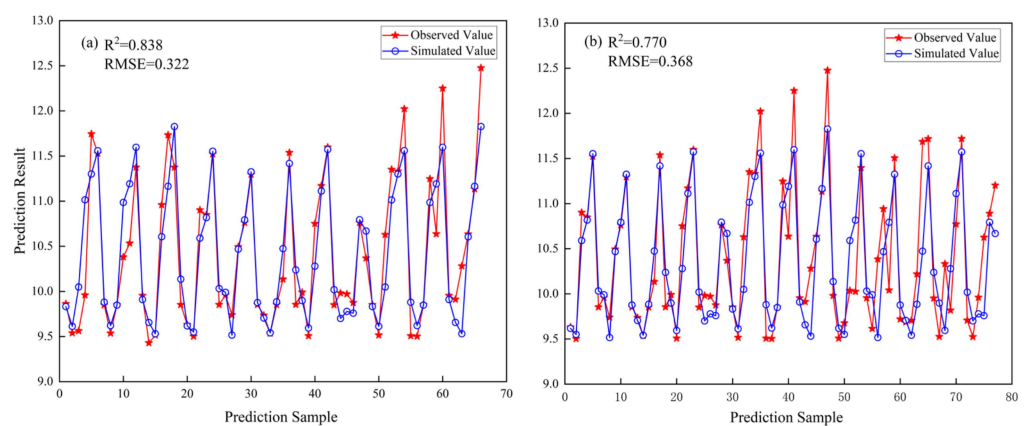


Figure 6. Comparison of predicted aboveground biomass: (a) LIBSVM proxy model training set; (b) testing set.

Using the prediction results, the first-order impact index (S) and total effect index (ST) were computed (Figure 7). Figure 7a illustrates the impact of different vegetation indices on predicting plant phosphorus concentration, while Figure 7b shows the corresponding indices for predicting aboveground biomass. Among the indices evaluated, MNVI exhibited the highest S and ST values in Figure 7a, indicating its significant direct and overall impact on predicting plant phosphorus concentrations, making it the most effective index for this parameter. In contrast, GSAVI showed the largest total effect and highest first-order index in Figure 7b, emphasizing its key role in the sensitivity analysis and its suitability as the optimal index for predicting the aboveground biomass. The vertical axes in both Figures represent the values of the S and ST for each vegetation index, providing a clear comparison of their contributions to the model predictions.

4.3. Diagnosis and Verification

Figures 8 and 9 illustrate the effectiveness of the vegetation index models and the derived PNI. The vegetation index models for phosphorus concentration (Figure 8a) and aboveground biomass (Figure 8b) were constructed using the optimal vegetation indices identified through the sensitivity analysis. Both models exhibited high coefficients of determination (R^2), confirming the reliability and robustness of the selected vegetation indices as strong predictors of phosphorus concentration and aboveground biomass. Figure 9 demonstrates the correlation between the estimated PNI, derived indirectly from plant phosphorus concentration and aboveground biomass, and the measured PNI. The estimated PNI values exhibited a strong linear relationship with the measured PNI, achieving

an R^2 value of 0.706 and an RMSE of 0.082. These results highlight the feasibility and accuracy of using this indirect method for PNI estimation, providing a valuable approach for assessing phosphorus nutritional status in maize.

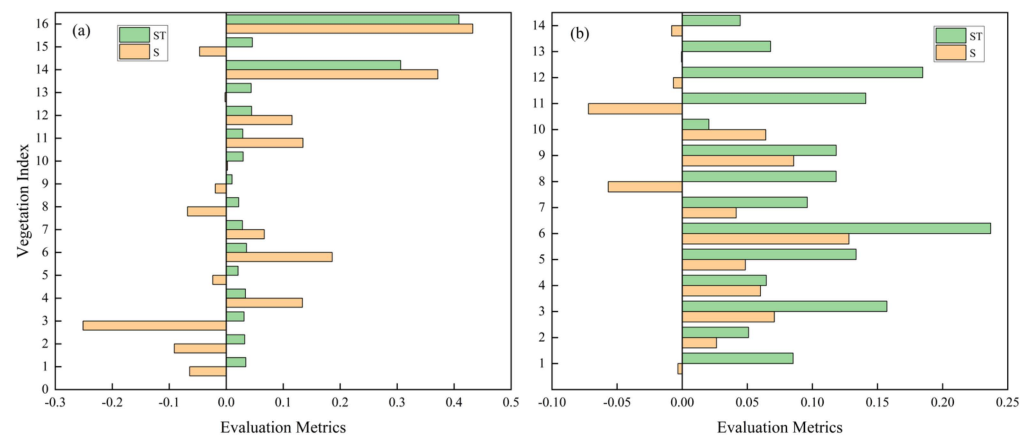


Figure 7. Evaluation metrics: (a) phosphorus concentration; (b) aboveground biomass.

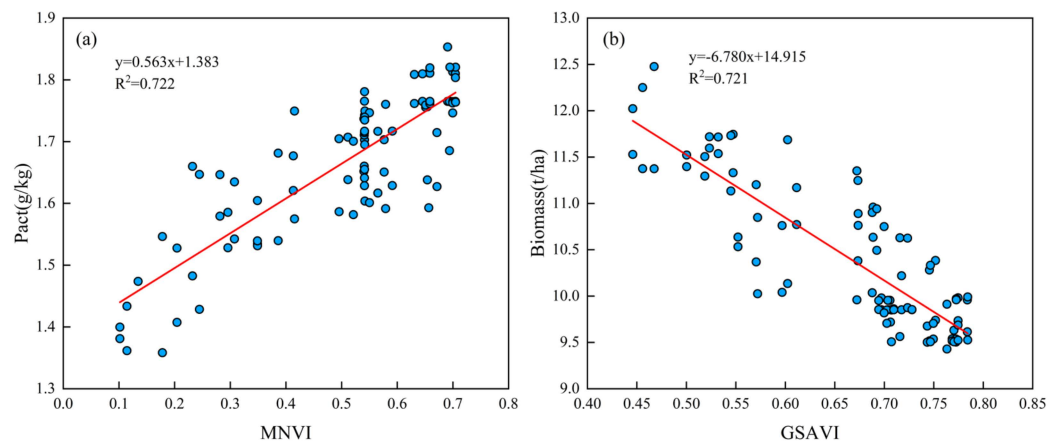


Figure 8. Phosphorus regression model constructed with the optimal vegetation index (a) and biomass regression model (b).

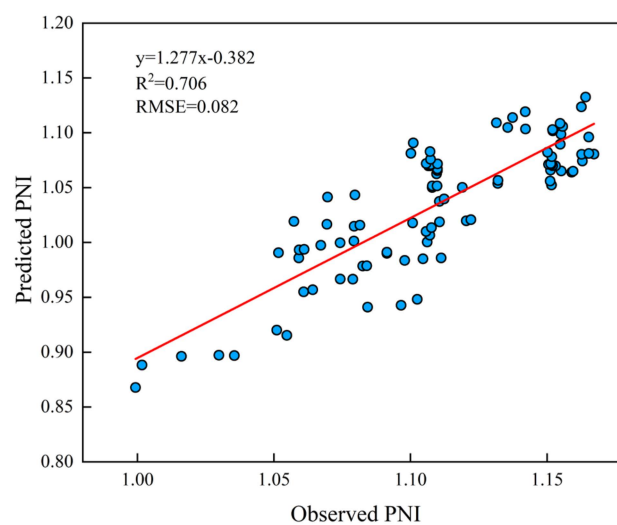


Figure 9. Relationship between observed and predicted PNI using MNVI-estimated P and GSAVI-estimated biomass.

The multispectral inversion model was applied to assess the spatial distribution of phosphorus status indicators in corn fields across Changchun. The spatial distribution

of the corn plant phosphorus concentration (Figure 10a) reveals minimal variation, with values predominantly between 1.2 and 1.5 g/kg. Similarly, the spatial distribution of aboveground biomass (Figure 10b) shows limited variation, with biomass values mostly ranging from 11 to 12.5 t/ha. The inversion model also provided an indirect estimate of the PNI for corn plants in the region (Figure 10c). The results indicate a generally uniform phosphorus nutrition status, with PNI values predominantly between 0.92 and 1.02, suggesting adequate phosphorus levels. Higher PNI values (1.02–1.12) were observed in some areas of northeastern Yushu. The phosphorus demand distribution, derived from the Pabs model (Figure 10d), confirms that phosphorus deficiency is uncommon, with most regions showing sufficient phosphorus levels, consistent with field survey results. The phosphorus demand was largely concentrated within the 0 to 8 kg/ha range. Areas identified as phosphorus-deficient were primarily located in northeastern Yushu, aligning with local phosphorus nutrition diagnoses. This deficiency is likely due to excessive phosphorus fertilization practices employed by farmers to ensure crop yields.

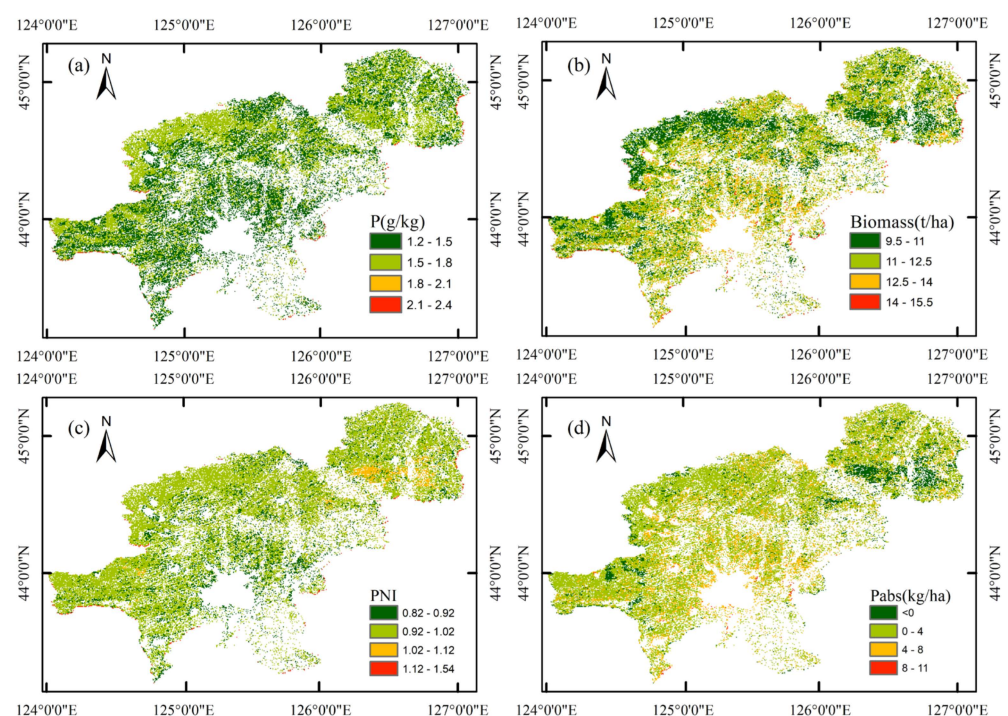


Figure 10. Examples of predicted corn P status indicators map at regional scale. (a) P; (b) biomass; (c) PNI; (d) Pabs, jointing stage in Changchun, China.

To assess the diagnostic accuracy of the remote sensing model for phosphorus nutrition, corn yield data were collected from 20 sampling points across corn-growing regions around Changchun. Some studies have shown a strong relationship between phosphorus fertilizer and maize yield. [48]. Accordingly, it is assumed that when the grain yield at a sampling point is lower than the local target yield, the phosphorus nutrition is considered deficient, while a yield meeting or exceeding the target indicates sufficient phosphorus nutrition. Sampling points where the PNI exceeds the target value (PNI_{target}) and the plant is not phosphorus-deficient, as well as those where PNI is below PNI_{target} and the plant exhibits phosphorus deficiency, are classified as correct diagnosis points (Figure 11). The correct diagnosis points, located in the first and third quadrants, account for 75% of all sampling points. This demonstrates that the model effectively identifies the phosphorus nutritional status of corn, confirming its strong applicability for phosphorus management.

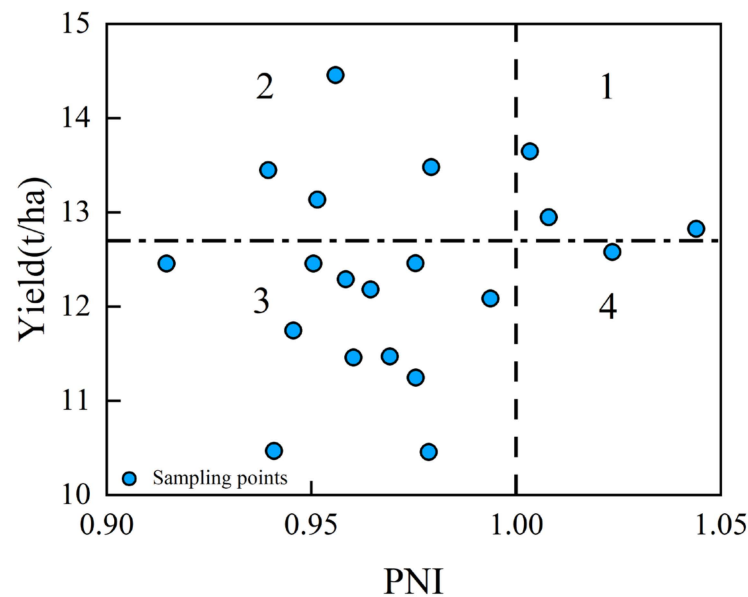


Figure 11. The relationship between PNI and maize yield.

5. Discussion

5.1. Application Differences in the Pabs Model Across Growth Stages

The Pabs model developed in this study to estimate maize phosphorus uptake across six growth stages demonstrates distinct advantages over previous approaches by addressing key limitations in existing research. Prior studies primarily relied on critical phosphorus concentration and phosphorus nutrition index [49] to evaluate crop phosphorus status. While these studies provided valuable insights, their methods were inherently qualitative, offering only a broad categorization of phosphorus status (e.g., deficiency or sufficiency) without the ability to quantify actual phosphorus uptake. This qualitative limitation restricts their applicability for precise nutrient management.

In contrast, our Pabs model provides a quantitative evaluation of maize phosphorus uptake, capturing phosphorus dynamics across different growth stages. The model achieves its highest accuracy during the jointing stage, surpassing the performance of previous methods. Moreover, this study highlights a critical advancement: the recognition that the optimal PNI is not static but varies across growth stages, typically peaking during the tasseling and silking stages and declining with plant maturation. By incorporating this variability, the Pabs model enhances its predictive capability and offers stage-specific insights, which were absent in earlier studies that relied on fixed PNI thresholds. Furthermore, while existing Pc-based methods focused on diagnosing phosphorus nutritional status qualitatively [50], the Pabs model enables precise, quantitative estimations of phosphorus uptake. This capability not only facilitates more accurate nutrient management decisions but also improves the understanding of phosphorus dynamics throughout the growth cycle. Compared to previous models, the Pabs model represents a significant advancement by combining qualitative diagnostic insights with quantitative precision.

In summary, the Pabs model addresses the limitations of existing methods by offering a more comprehensive and accurate evaluation of maize phosphorus nutrition. Its ability to quantitatively assess phosphorus uptake at a regional scale, coupled with its stage-specific adaptability, makes it a superior tool for improving phosphorus management strategies and optimizing maize production in different agricultural systems.

5.2. Estimation of Corn Phosphorus Status Indicators

Phosphorus is an essential element for crop growth, playing a crucial role in the composition of proteins, phospholipids, enzymes, and nucleic acids. Additionally, phosphorus is integral to metabolic processes such as carbohydrate synthesis, transport, and photosynthesis, including photophosphorylation, sucrose phosphate transport, and cell division [51–53]. The role of phosphorus in these biochemical pathways significantly impacts the spectral characteristics of crops. Specifically, chemical bond changes, such as those involving N-H and O-H bonds induced by light exposure, alter light absorption and reflection, producing distinct spectral curves that reflect the crop's phosphorus status [54].

Crop sensitivity to phosphorus is primarily observed in the near-infrared (NIR) spectral region, as phosphorus's key role in photosynthetic activity is closely associated with structural indicators like biomass and leaf area index (LAI) [55]. However, studies have shown that phosphorus-responsive wavelengths are distributed across both visible and near-infrared regions. Research by Ayala-Silva and Beyl demonstrated a significant reduction in chlorophyll content in wheat under phosphorus and potassium deficiency conditions. This reduction is primarily attributed to phosphorus's critical influence on crop chlorophyll and anthocyanin content [56]. Phosphorus deficiency typically leads to increased anthocyanin accumulation [57], which produces specific spectral responses in the 550 nm green light region and the 700 nm red-edge region [58]. The intensity of these spectral peaks is directly correlated with anthocyanin concentration, resulting in decreased spectral reflectance as anthocyanin levels increase [59]. Furthermore, the green light region (540–560 nm) and the red to red-edge region (640–760 nm) are particularly sensitive to anthocyanin concentration, underscoring their potential for monitoring phosphorus nutritional status [60,61].

In this study, vegetation indices related to the phosphorus nutritional status of maize were primarily derived from combinations of visible and near-infrared bands. The inversion accuracy of these indices exceeded 0.70, indirectly demonstrating the potential of combining visible and NIR bands to monitor maize phosphorus status. This potential arises from the significant impact of phosphorus application on maize chlorophyll, anthocyanin, biomass, and other structural canopy indices.

5.3. Challenges and Future Research Needs

The current model demonstrates significant potential for assessing phosphorus nutritional status in maize, but its broader applicability to other crops with similar physiological structures remains uncertain. Future research should focus on adapting this model to a wider range of crops by considering variations in plant morphology and nutrient uptake patterns, thereby enhancing its versatility and enabling its integration into diverse agricultural systems.

Additionally, satellite imagery from platforms like Sentinel-2 provides valuable data, but its spatial and temporal resolution is insufficient for identifying phosphorus deficiencies at the field level. Since farmers make fertilizer application decisions at different growth stages, relying solely on satellite data for such critical decisions is impractical. Meanwhile, the model is also influenced by climate conditions, as fluctuations in temperature and weather events, such as rain, can complicate satellite data collection and impact crop growth. To mitigate these challenges, drone-based low-altitude remote sensing can be employed to provide more frequent and precise image acquisition throughout the crop's growth cycle. Drones offer a valuable supplement to satellite data, enabling more accurate and timely assessments of phosphorus status. Furthermore, the use of high-temporal-resolution satellites, such as FORMOSAT-2, which revisits daily and provides enhanced spatial and temporal resolution compared to Sentinel-2, could significantly improve large-

scale agricultural monitoring. The final fertilization prescription maps for maize could also be integrated with yield-monitoring equipment to enable more effective applications at the field scale. By combining these technologies, the model's reliability and practicality for phosphorus management can be further enhanced.

6. Conclusions

This study achieved the remote sensing inversion of plant phosphorus concentration and aboveground biomass using field data and Sobol sensitivity analysis. Key findings demonstrate that the Pabs diagnostic model provides accurate quantitative estimation of phosphorus absorption in corn. Using PNI, a diagnostic model of Pabs was developed to estimate phosphorus demand at the regional level, revealing sufficient phosphorus levels across most areas of Changchun, with a phosphorus deficiency identified only in northeastern Yushu. Field validation indicated a 75% accuracy rate for the remote sensing diagnosis, underscoring the model's applicability for regional-scale phosphorus demand estimation in corn cultivation. Additionally, the phosphorus nutrition diagnosis model effectively estimates the phosphorus nutritional status of corn. The Sobol sensitivity analysis identified the vegetation index with the highest correlation, which was utilized to construct multispectral inversion models for these parameters. The R^2 values of 0.722 for phosphorus concentration and 0.721 for aboveground biomass confirmed the adequacy of remote sensing-based parameter estimation. These inversion results were applied within the phosphorus diagnostic model, yielding an R^2 of 0.706 and an RMSE of 0.082 for the PNI, demonstrating the model's effectiveness in accurately estimating corn phosphorus nutritional status.

Author Contributions: Conceptualization, X.Z.; methodology, X.Z. and Y.X.; software, X.Z. and Z.W.; validation, X.Z., Y.X. and Z.W.; writing—original draft preparation, X.Z.; writing—review and editing, S.C. and Z.W.; funding acquisition, S.C. All authors have read and agreed to the published version of the manuscript.

Funding: This research was funded by the Changchun Satellite and Application Industry Major Science and Technology Project (grant No. 2024WX06).

Institutional Review Board Statement: Not applicable.

Informed Consent Statement: Not applicable.

Data Availability Statement: The multispectral data used in this study for calculating vegetation indices are available from Google Earth Engine at <https://earthengine.google.com/>, accessed on 1 July 2024. For maize classification in Changchun, a 10 m resolution crop type map was utilized, derived from Sentinel-2 imagery and processed using a random forest algorithm on the Google Earth Engine platform. Climate data, were retrieved from the China Meteorological Administration platform at <http://data.cma.cn/>, accessed on 1 May 2024.

Conflicts of Interest: The authors declare no conflicts of interest.

References

1. Hawkesford, M.J.; Cakmak, I.; Coskun, D.; De Kok, L.J.; Lambers, H.; Schjoerring, J.K.; White, P.J. Functions of macronutrients. In *Marschner's Mineral Nutrition of Plants*; Elsevier: Amsterdam, The Netherlands, 2023; pp. 201–281.
2. Lambers, H. Phosphorus acquisition and utilization in plants. *Annu. Rev. Plant Biol.* **2022**, *73*, 17–42. [[CrossRef](#)] [[PubMed](#)]
3. George, T.S.; Hinsinger, P.; Turner, B.L. Phosphorus in soils and plants—facing phosphorus scarcity. *Plant Soil* **2016**, *401*, 1–6. [[CrossRef](#)]
4. Shen, J.; Yuan, L.; Zhang, J.; Li, H.; Bai, Z.; Chen, X.; Zhang, W.; Zhang, F. Phosphorus dynamics: From soil to plant. *Plant Physiol.* **2011**, *156*, 997–1005. [[CrossRef](#)] [[PubMed](#)]
5. Isidra-Arellano, M.C.; Delaux, P.-M.; Valdés-López, O. The phosphate starvation response system: Its role in the regulation of plant–microbe interactions. *Plant Cell Physiol.* **2021**, *62*, 392–400. [[CrossRef](#)] [[PubMed](#)]

6. Jezeq, M.; Allan, A.C.; Jones, J.J.; Geilfus, C.M. Why do plants blush when they are hungry? *New Phytol.* **2023**, *239*, 494–505. [CrossRef]
7. Lopez, G.; Ahmadi, S.H.; Amelung, W.; Athmann, M.; Ewert, F.; Gaiser, T.; Gocke, M.I.; Kautz, T.; Postma, J.; Rachmilevitch, S. Nutrient deficiency effects on root architecture and root-to-shoot ratio in arable crops. *Front. Plant Sci.* **2023**, *13*, 1067498. [CrossRef]
8. Abobatta, W.; Abd Alla, M. Role of phosphates fertilizers in sustain horticulture production: Growth and productivity of vegetable crops. *Asian J. Agric. Res.* **2023**, *2*, 1. [CrossRef]
9. Gómez, M.I.; Magnitskiy, S.; Rodríguez, L.E. Critical dilution curves for nitrogen, phosphorus, and potassium in potato group Andigenum. *Agron. J.* **2019**, *111*, 419–427. [CrossRef]
10. Bélanger, G.; Ziadi, N.; Pageau, D.; Grant, C.; Högnäsbacka, M.; Virkajärvi, P.; Hu, Z.; Lu, J.; Lafond, J.; Nyiraneza, J. A model of critical phosphorus concentration in the shoot biomass of wheat. *Agron. J.* **2015**, *107*, 963–970. [CrossRef]
11. Zamuner, E.C.; Lloveras, J.; Echeverría, H.E. Use of a critical phosphorus dilution curve to improve potato crop nutritional management. *Am. J. Potato Res.* **2016**, *93*, 392–403. [CrossRef]
12. Pang, B.-G.; Cao, N.; Zhou, Z.-G.; Zhao, W.-Q. Critical phosphorus concentration dilution model and phosphorus nutrition diagnosis in two cotton cultivars with different phosphorus sensitivity. *Sci. Agric. Sin.* **2020**, *53*, 4561–6130.
13. Bélanger, G.; Ziadi, N. Phosphorus and nitrogen relationships during spring growth of an aging timothy sward. *Agron. J.* **2008**, *100*, 1757–1762. [CrossRef]
14. Lapaz Oliveira, A.M.; Castro-Franco, M.; Saínez Rozas, H.R.; Carciochi, W.D.; Balzarini, M.; Avila, O.; Ciampitti, I.; Reussi Calvo, N.I. Monitoring corn nitrogen nutrition index from optical and synthetic aperture radar satellite data and soil available nitrogen. *Precis. Agric.* **2023**, *24*, 2592–2606. [CrossRef]
15. Cao, Q.; Miao, Y.; Feng, G.; Gao, X.; Li, F.; Liu, B.; Yue, S.; Cheng, S.; Ustin, S.L.; Khosla, R. Active canopy sensing of winter wheat nitrogen status: An evaluation of two sensor systems. *Comput. Electron. Agric.* **2015**, *112*, 54–67. [CrossRef]
16. Yao, Y.; Miao, Y.; Cao, Q.; Wang, H.; Gnyp, M.L.; Bareth, G.; Khosla, R.; Yang, W.; Liu, F.; Liu, C. In-season estimation of rice nitrogen status with an active crop canopy sensor. *IEEE J. Sel. Top. Appl. Earth Obs. Remote Sens.* **2014**, *7*, 4403–4413. [CrossRef]
17. Houles, V.; Guerif, M.; Mary, B. Elaboration of a nitrogen nutrition indicator for winter wheat based on leaf area index and chlorophyll content for making nitrogen recommendations. *Eur. J. Agron.* **2007**, *27*, 1–11. [CrossRef]
18. Mali, G.R.; Khan, T.; Pagaria, P.; Choudhary, H.; Jat, B.L. Knowledge and attitude of farmers for conducting soil analysis. *J. Exp. Agric. Int* **2022**, *44*, 47–50. [CrossRef]
19. Mallarino, A.; Sawyer, J. Phosphorus and Potassium Tissue Testing in Corn and Soybean. 2018. Available online: <https://store.extension.iastate.edu/product/Phosphorus-and-Potassium-Tissue-Testing-in-Corn-and-Soybean> (accessed on 27 November 2024).
20. Havlin, J.L.; Tisdale, S.L.; Nelson, W.L.; Beaton, J.D. *Soil Fertility and Fertilizers*; Pearson Education India: Noida, India, 2016.
21. Drusch, M.; Del Bello, U.; Carlier, S.; Colin, O.; Fernandez, V.; Gascon, F.; Hoersch, B.; Isola, C.; Laberinti, P.; Martimort, P. Sentinel-2: ESA's optical high-resolution mission for GMES operational services. *Remote Sens. Environ.* **2012**, *120*, 25–36. [CrossRef]
22. You, N.; Dong, J.; Huang, J.; Du, G.; Zhang, G.; He, Y.; Yang, T.; Di, Y.; Xiao, X. The 10-m crop type maps in Northeast China during 2017–2019. *Sci. Data* **2021**, *8*, 41. [CrossRef]
23. Cichota, R.; Vogeler, I.; Sharp, J.; Verburg, K.; Huth, N.; Holzworth, D.; Dalgliesh, N.; Snow, V. A protocol to build soil descriptions for APSIM simulations. *MethodsX* **2021**, *8*, 101566. [CrossRef]
24. Tucker, C.J. Red and photographic infrared linear combinations for monitoring vegetation. *Remote Sens. Environ.* **1979**, *8*, 127–150. [CrossRef]
25. Buschmann, C.; Nagel, E. In vivo spectroscopy and internal optics of leaves as basis for remote sensing of vegetation. *Int. J. Remote Sens.* **1993**, *14*, 711–722. [CrossRef]
26. Gitelson, A.A.; Kaufman, Y.J.; Merzlyak, M.N. Use of a green channel in remote sensing of global vegetation from EOS-MODIS. *Remote Sens. Environ.* **1996**, *58*, 289–298. [CrossRef]
27. Roujean, J.-L.; Breon, F.-M. Estimating PAR absorbed by vegetation from bidirectional reflectance measurements. *Remote Sens. Environ.* **1995**, *51*, 375–384. [CrossRef]
28. Gitelson, A.A. Wide dynamic range vegetation index for remote quantification of biophysical characteristics of vegetation. *J. Plant Physiol.* **2004**, *161*, 165–173. [CrossRef]
29. Huete, A.R. A soil-adjusted vegetation index (SAVI). *Remote Sens. Environ.* **1988**, *25*, 295–309. [CrossRef]
30. Rondeaux, G.; Steven, M.; Baret, F. Optimization of soil-adjusted vegetation indices. *Remote Sens. Environ.* **1996**, *55*, 95–107. [CrossRef]
31. Chen, J.M. Evaluation of vegetation indices and a modified simple ratio for boreal applications. *Can. J. Remote Sens.* **1996**, *22*, 229–242. [CrossRef]
32. Qi, J.; Chehbouni, A.; Huete, A.R.; Kerr, Y.H.; Sorooshian, S. A modified soil adjusted vegetation index. *Remote Sens. Environ.* **1994**, *48*, 119–126. [CrossRef]

33. Datt, B. Visible/near infrared reflectance and chlorophyll content in Eucalyptus leaves. *Int. J. Remote Sens.* **1999**, *20*, 2741–2759. [\[CrossRef\]](#)
34. Wang, W.; Yao, X.; Yao, X.; Tian, Y.; Liu, X.; Ni, J.; Cao, W.; Zhu, Y. Estimating leaf nitrogen concentration with three-band vegetation indices in rice and wheat. *Field Crops Res.* **2012**, *129*, 90–98. [\[CrossRef\]](#)
35. Sims, D.A.; Gamon, J.A. Relationships between leaf pigment content and spectral reflectance across a wide range of species, leaf structures and developmental stages. *Remote Sens. Environ.* **2002**, *81*, 337–354. [\[CrossRef\]](#)
36. Gitelson, A.A.; Kaufman, Y.J.; Stark, R.; Rundquist, D. Novel algorithms for remote estimation of vegetation fraction. *Remote Sens. Environ.* **2002**, *80*, 76–87. [\[CrossRef\]](#)
37. Penuelas, J.; Baret, F.; Filella, I. Semi-empirical indices to assess carotenoids/chlorophyll a ratio from leaf spectral reflectance. *Photosynthetica* **1995**, *31*, 221–230.
38. Gong, P.; Pu, R.; Biging, G.S.; Larrieu, M.R. Estimation of forest leaf area index using vegetation indices derived from Hyperion hyperspectral data. *IEEE Trans. Geosci. Remote Sens.* **2003**, *41*, 1355–1362. [\[CrossRef\]](#)
39. Broge, N.H.; Leblanc, E. Comparing prediction power and stability of broadband and hyperspectral vegetation indices for estimation of green leaf area index and canopy chlorophyll density. *Remote Sens. Environ.* **2001**, *76*, 156–172. [\[CrossRef\]](#)
40. Haboudane, D.; Miller, J.R.; Pattey, E.; Zarco-Tejada, P.J.; Strachan, I.B. Hyperspectral vegetation indices and novel algorithms for predicting green LAI of crop canopies: Modeling and validation in the context of precision agriculture. *Remote Sens. Environ.* **2004**, *90*, 337–352. [\[CrossRef\]](#)
41. Huete, A.; Didan, K.; Miura, T.; Rodriguez, E.P.; Gao, X.; Ferreira, L.G. Overview of the radiometric and biophysical performance of the MODIS vegetation indices. *Remote Sens. Environ.* **2002**, *83*, 195–213. [\[CrossRef\]](#)
42. Haboudane, D.; Tremblay, N.; Miller, J.R.; Vigneault, P. Remote estimation of crop chlorophyll content using spectral indices derived from hyperspectral data. *IEEE Trans. Geosci. Remote Sens.* **2008**, *46*, 423–437. [\[CrossRef\]](#)
43. Daughtry, C.S.; Walthall, C.; Kim, M.; De Colstoun, E.B.; McMurtrey Iii, J. Estimating corn leaf chlorophyll concentration from leaf and canopy reflectance. *Remote Sens. Environ.* **2000**, *74*, 229–239. [\[CrossRef\]](#)
44. Haboudane, D.; Miller, J.R.; Tremblay, N.; Zarco-Tejada, P.J.; Dextraze, L. Integrated narrow-band vegetation indices for prediction of crop chlorophyll content for application to precision agriculture. *Remote Sens. Environ.* **2002**, *81*, 416–426. [\[CrossRef\]](#)
45. Eitel, J.; Long, D.; Gessler, P.; Smith, A. Using in-situ measurements to evaluate the new RapidEye™ satellite series for prediction of wheat nitrogen status. *Int. J. Remote Sens.* **2007**, *28*, 4183–4190. [\[CrossRef\]](#)
46. Delve, R.J.; Probert, M.; Cobo, J.; Ricaurte, J.; Rivera, M.; Barrios, E.; Rao, I.M. Simulating phosphorus responses in annual crops using APSIM: Model evaluation on contrasting soil types. *Nutr. Cycl. Agroecosyst.* **2009**, *84*, 293–306. [\[CrossRef\]](#)
47. Wang, X.; Shen, J.; Liao, H. Acquisition or utilization, which is more critical for enhancing phosphorus efficiency in modern crops? *Plant Sci.* **2010**, *179*, 302–306. [\[CrossRef\]](#)
48. Purwanto, B.H.; Wulandari, P.; Sulistyaningsih, E.; Utami, S.N.; Handayani, S. Improved corn yields when humic acid extracted from composted manure is applied to acid soils with phosphorus fertilizer. *Appl. Environ. Soil Sci.* **2021**, *2021*, 8838420. [\[CrossRef\]](#)
49. Gagnon, B.; Ziadi, N.; Bélanger, G.; Parent, G. Validation and use of critical phosphorus concentration in maize. *Eur. J. Agron.* **2020**, *120*, 126147. [\[CrossRef\]](#)
50. Xie, Y.; Li, Y.; Wang, L.; Nizamani, M.M.; Lv, Z.; Dang, Z.; Li, W.; Qi, Y.; Zhao, W.; Zhang, J. Determination of Critical Phosphorus Dilution Curve Based on Capsule Dry Matter for Flax in Northwest China. *Agronomy* **2022**, *12*, 2819. [\[CrossRef\]](#)
51. Li, B.; Liew, O.W.; Asundi, A.K. Pre-visual detection of iron and phosphorus deficiency by transformed reflectance spectra. *J. Photochem. Photobiol. B Biol.* **2006**, *85*, 131–139. [\[CrossRef\]](#)
52. Pimstein, A.; Karnieli, A.; Bansal, S.K.; Bonfil, D.J. Exploring remotely sensed technologies for monitoring wheat potassium and phosphorus using field spectroscopy. *Field Crops Res.* **2011**, *121*, 125–135. [\[CrossRef\]](#)
53. Wang, J.; Shi, T.; Liu, H.; Wu, G. Successive projections algorithm-based three-band vegetation index for foliar phosphorus estimation. *Ecol. Indic.* **2016**, *67*, 12–20. [\[CrossRef\]](#)
54. Liu, Y.; Feng, H.; Yue, J.; Jin, X.; Fan, Y.; Chen, R.; Bian, M.; Ma, Y.; Li, J.; Xu, B. Improving potato AGB estimation to mitigate phenological stage impacts through depth features from hyperspectral data. *Comput. Electron. Agric.* **2024**, *219*, 108808. [\[CrossRef\]](#)
55. Ayala-Silva, T.; Beyl, C.A. Changes in spectral reflectance of wheat leaves in response to specific macronutrient deficiency. *Adv. Space Res.* **2005**, *35*, 305–317. [\[CrossRef\]](#) [\[PubMed\]](#)
56. Zhang, Y.; Wang, T.; Li, Z.; Wang, T.; Cao, N. Based on machine learning algorithms for estimating leaf phosphorus concentration of rice using optimized spectral indices and continuous wavelet transform. *Front. Plant Sci.* **2023**, *14*, 1185915. [\[CrossRef\]](#) [\[PubMed\]](#)
57. Jiang, C.; Gao, X.; Liao, L.; Harberd, N.P.; Fu, X. Phosphate starvation root architecture and anthocyanin accumulation responses are modulated by the gibberellin-DELLA signaling pathway in Arabidopsis. *Plant Physiol.* **2007**, *145*, 1460–1470. [\[CrossRef\]](#) [\[PubMed\]](#)
58. Gitelson, A.A.; Merzlyak, M.N.; Chivkunova, O.B. Optical properties and nondestructive estimation of anthocyanin content in plant leaves. *Photochem. Photobiol. B Biol.* **2001**, *74*, 38–45. [\[CrossRef\]](#)

59. Liu, X.; Shen, J.; Chang, Q.; Yan, L.; Gao, Y.; Xie, F. Prediction of anthocyanin content in peony leaves based on visible/near-infrared spectra. *Trans. Chin. Soc. Agric. Mach.* **2015**, *46*, 319–324.
60. Gitelson, A.A.; Keydan, G.P.; Merzlyak, M.N. Three-band model for noninvasive estimation of chlorophyll, carotenoids, and anthocyanin contents in higher plant leaves. *Geophys. Res. Lett.* **2006**, *33*. [[CrossRef](#)]
61. Merzlyak, M.N.; Solovchenko, A.E.; Gitelson, A.A. Reflectance spectral features and non-destructive estimation of chlorophyll, carotenoid and anthocyanin content in apple fruit. *Postharvest Biol. Technol.* **2003**, *27*, 197–211. [[CrossRef](#)]

Disclaimer/Publisher’s Note: The statements, opinions and data contained in all publications are solely those of the individual author(s) and contributor(s) and not of MDPI and/or the editor(s). MDPI and/or the editor(s) disclaim responsibility for any injury to people or property resulting from any ideas, methods, instructions or products referred to in the content.